Letter

Multiple Zeeman-type hidden spin splittings in $\mathcal{PT}$-symmetric layered antiferromagnets

Sajjan Sheoran [*] and Saswata Bhattacharya [†]
Department of Physics, Indian Institute of Technology Delhi, New Delhi 110016, India

(Received 7 September 2023; revised 18 December 2023; accepted 2 January 2024; published 16 January 2024)

Centrosymmetric antiferromagnetic semiconductors, although abundant in nature, appear less favorable in spintronics owing to the lack of inherent spin polarization and magnetization. We unveil hidden Zeeman-type spin splitting in layered centrosymmetric antiferromagnets with asymmetric sublayer structures through first-principles simulations and symmetry analysis. Taking the bilayer counterpart of recently synthesized monolayer MnSe, we demonstrate that the degenerate states around specific $\boldsymbol{k}$ points spatially segregate on different sublayers forming $\mathcal{PT}$-symmetric pairs. Furthermore, degenerate states exhibit uniform in-plane spin configurations with opposite orientations enforced by mirror symmetry. Bands are locally Zeeman split up to order of $\sim$70 meV. Strikingly, a tiny electric field of a few mVÅ^{-1} along the z direction breaks the double degeneracy forming additional Zeeman pairs. The design principle to obtain Zeeman-type splitting in centrosymmetric antiferromagnets established here expands the range of materials among which to look for spintronics.

DOI: 10.1103/PhysRevB.109.L020404

Introduction. Spin polarization in nonmagnetic crystals without inversion symmetry ($\mathcal{P}$) can be achieved through relativistic spin-orbit coupling (SOC), as demonstrated by Dresselhaus [1] and Rashba [2–4] in their influential works. Recent research has indicated that a similar phenomenon called hidden spin polarization (HSP) can exist even in centrosymmetric crystals, provided that individual atomic sites break local inversion symmetry [5–10]. The discovery of HSP opens up possibilities for a broader range of materials in spintronics and offers new insights into various hidden physical properties such as optical polarization [11,12], valley polarization [12], orbital polarization [13,14], and Berry curvature [15,16]. The HSP effect in nonmagnetic materials, characterized by the coexistence of $\mathcal{P}$ and time-reversal symmetry ($\mathcal{T}$), is odd distributed in both real ($\boldsymbol{r}$) and momentum ($\boldsymbol{k}$) spaces within a localized sector [17]. While techniques like spin- and angle-resolved photoemission spectroscopy have successfully measured HSP with both $\boldsymbol{r}$ and $\boldsymbol{k}$ resolution, its application in spintronics necessitates the breaking of global symmetry, typically achieved through external electric fields [8,12].

Antiferromagnets have recently emerged as a viable substitute for nonmagnetic and ferromagnetic materials in spintronic applications [18–22]. Due to their resilience against magnetic disruptions, lack of stray fields, and ability to exhibit exceptionally rapid spin dynamics, antiferromagnets possess the potential to outperform ferromagnets. Recent research focused on investigating spin splittings within various magnetic space groups, encompassing antiferromagnets [23,24]. However, centrosymmetric antiferromagnetic (AFM) semiconductors, which lack polarization and magnetization, pose challenges in generating substantial and controllable spin splitting using magnetic or electric fields [25–27]. As a result, despite their abundance in nature, centrosymmetric AFM semiconductors do not appear promising for practical applications in spintronics. Interestingly, the magnetoelectric effect [28], in which an electric field has a dual effect of inducing both polarization and magnetization, allows control over spin splitting and textures in centrosymmetric antiferromagnets even without SOC [27]. The gate-controlled magneto-optic Kerr effect in layered collinear AFM $MnPSe_3$ [25] and the anomalous Hall effect in AFM CuMnAs [29] are observed. Even though the magnetoelectric coupling effect is observed in several centrosymmetric antiferromagnets [25–27,29], the attainment of HSP remains uncommon due to the stringent requirements imposed on lattice and site symmetry.

This Letter examines the hidden Zeeman-type spin splitting (HZSS) in $\mathcal{PT}$-symmetric AFM two-dimensional (2D) materials originating from specific local sites asymmetries. We perform symmetry analysis and density-functional theory (DFT) calculations on prototypical layered MnSe to show that doubly degenerate states with opposite spin polarization are segregated on different sublayers connected through $\mathcal{PT}$ symmetry. The specific states from a single layer are locally Zeeman split, exhibiting a unique spin-sublayer locking effect. In addition, the mirror plane (M_x) enforces the spins to be $\boldsymbol{k}$ independent. Strikingly, a tiny electric field splits the otherwise doubly degenerate bands, preserving the spin configurations. Switching the electric field can reverse the electronic spin magnetization connected to the energy level splitting.

Methods. DFT calculations are performed using the projector-augmented wave method [30] as implemented in the VASP [31] package. The Perdew-Burke-Ernzerhof-based generalized-gradient approximation [32] with a Hubbard U correction [33] is adopted to describe electronic interaction. Following Refs [34–36], we select an effective U of 2.3 eV for Mn-d orbitals, giving a reasonable band gap of 1.82 eV

[*] phz198687@physics.iitd.ac.in
[†] saswata@physics.iitd.ac.in

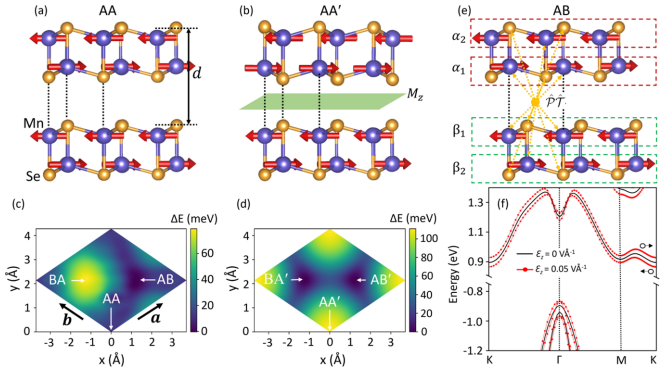

FIG. 1. Geometric structures of bilayer MnSe with high-symmetry stackings (a) AA and (b) AA′. The upper layer in AA and AA′ is obtained by the translation ($d\hat{z}$) and mirror reflection (M_z) of the lower layer, respectively. The energy distribution of different translations between layers for the (c) AA and (d) AA′ stacking. The energy surfaces are interpolated using ten steps in $\boldsymbol{a}$ and $\boldsymbol{b}$ directions such that all possible high-symmetry stackings are included. (e) Structure of the global ground state with AB stacking having magnetization $M\uparrow\downarrow\uparrow\downarrow$. The sublayers α_i and β_i ($i = 1, 2$) are connected by the $\mathcal{PT}$ center with orange dashed lines. (f) Energy band dispersion of monolayer MnSe without (solid black lines) and with an electric field (red dashed lines) of 0.05 VÅ^{-1} along the z direction.

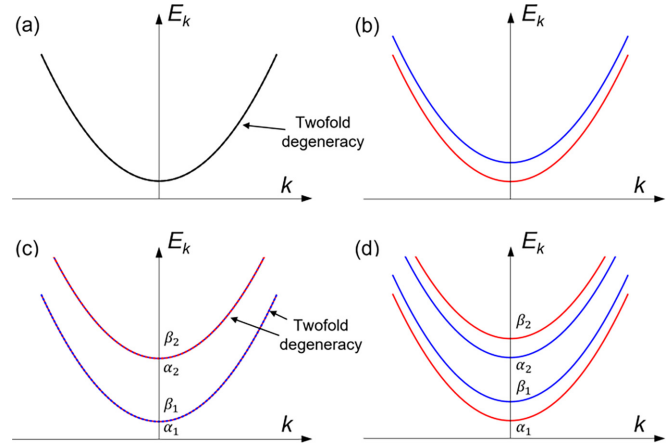

FIG. 2. Schematic illustration of band structures with (a) null spin splitting and (b) Zeeman spin splitting. (c) Sketches of twofold degenerate bands in the presence of $\mathcal{PT}$ symmetry with hidden spin polarization, where each band is segregated on different sublayers. (d) The lifting of band degeneracy in the presence of an electric field along the z direction. The energy levels with positive and negative spin magnetization are sketched in the red and blue curves, respectively.

for monolayer MnSe. Note that we have computed band structure in the framework of noncollinear magnetism with SOC, although spin splittings are SOC independent. The gate-controlled electric field is applied using the approach introduced by Neugebauer and Scheffler [37]. Methods are detailed in Sec. I of the Supplemental Material (SM) [38].

Monolayer MnSe. The MnSe monolayer consists of two buckled honeycomb sublayers of MnSe, interconnected by Mn-Se bonds [Fig. 1(a)]. Within the monolayer, the upper Mn/Se atoms are positioned alternately on top of the lower Se/Mn atoms. Each unit cell of monolayer contains two Mn and two Se atoms, with a lattice constant of 4.28 Å, belonging to the space group $P\bar{3}m1$ with $\mathcal{P}$ symmetry (ignoring spin configurations). Considering different possible magnetic configurations, we find that the upper and lower sublayers are coupled antiferromagnetically through Néel-type antiferromagnetism. The robust Néel-type AFM state is more stable than the FM state by 0.38 eV per unit cell (u.c.). Additionally, the magnetic anisotropic energy (MAE) calculations reveal that the monolayer MnSe prefers in-plane magnetization over out-of-plane magnetization, with an energy difference of 0.37 meV/u.c. These results are consistent with the previous experimental [34] and theoretical reports [34–36].

Bilayer stackings. Determination of stacking orders in multilayers is challenging, especially for more complex structures. First, we created bilayer MnSe by taking the upper layer as translation (by $d\hat{z}$) and mirror reflection (M_z) of the lower layer, as shown in Figs. 1(a) and 1(b). We name these stacking AA (obtained through $d\hat{z}$) and AA′ (obtained through M_z), following the nomenclature used in Ref. [39]. After that, we transformed these stackings into other possible high-symmetry stackings by translation sliding of one of the basal planes in the unit cell: going to AB and BA state from AA, and going to AB′ and BA′ from AA′. Further, DFT calculations were conducted to ascertain the lowest energy states for various stacking arrangements (see Sec. I of SM [38] for relaxed structures and discussion). As shown in Fig. 1(c), translating the top layer in AA by $\frac{2}{3}\boldsymbol{a} + \frac{1}{3}\boldsymbol{b}$ results in AB stacking with nondegenerate global energy minimum. In comparison, BA stacking is energetically unfavorable. On the other hand, shifting the top layer from AA′ leads to doubly degenerate energy minima AB′ and BA′ [Fig. 1(d)]. AB stacking is energetically most favorable, having lower energy than AB′/BA′ by 14 meV per unit cell. Bilayer MnSe can be divided into sublayers α_i and β_i ($i = 1, 2$), each sublayer containing a single Mn atom. Note that we have taken four nondegenerate magnetic configurations $M\uparrow\uparrow\uparrow\uparrow$, $M\uparrow\downarrow\uparrow\downarrow$, $M\uparrow\downarrow\downarrow\uparrow$, and $M\uparrow\uparrow\downarrow\downarrow$ (here, up and down arrows represent the magnetic moment direction of sublayers along $+x$ and $-x$ directions, respectively, in the order of β_2, β_1, α_1, and α_2 [Fig. 1(e)]). Given that the easy axis of magnetization lies in the x-y plane with MAE of 0.9 meV/u.c., we have chosen the x direction as the axis for magnetization. Our DFT calculations show that Néel-type AFM configuration $M\uparrow\downarrow\uparrow\downarrow$ has the lowest energy. Therefore, our calculation assumes that the bilayer MnSe exhibits AB stacking with $M\uparrow\downarrow\uparrow\downarrow$ configuration unless otherwise specified.

Symmetry analysis. $\mathcal{PT}$ symmetry flips the spin but retains the $\boldsymbol{k}$ invariance, i.e., $\mathcal{PT}(\boldsymbol{k}, \boldsymbol{\sigma}) = \mathcal{P}E(-\boldsymbol{k}, -\boldsymbol{\sigma}) = E(\boldsymbol{k}, -\boldsymbol{\sigma})$, enforcing the spin degeneracy. Therefore, energy bands are doubly degenerate without spin polarization locally and globally if all atomic sites are $\mathcal{PT}$ symmetric [Fig. 2(a)]. Broken $\mathcal{PT}$ symmetry, i.e., in ferromagnetic or noncentrosymmetric AFM materials, leads to the Zeeman spin splittings [Fig. 2(b)] [20]. The magnetic point group (MPG) for bilayer MnSe with AB stacking is $2'/m$, having symmetry operations M_x, $C_{2x}\mathcal{T}$, and $\mathcal{PT}$ besides trivial identity operation (I). Here, M_x and C_{2x} are mirror reflection in the

y-z plane and twofold rotation around the x axis, respectively. Bilayer MnSe is globally centrosymmetric (D_{3d}). However, the atomic site symmetries of Mn (C_{3v}) and Se (C_{3v}) are noncentrosymmetric. MPG of each sublayer (α_i, β_i) contains I and M_x. While the total spin polarization is prohibited by global $\mathcal{PT}$ symmetry, the $\mathcal{PT}$-asymmetric nature of sublayers allows the observation of spin polarization locally dubbed hidden spin polarization. The α_i sublayer is connected to the β_i sublayer through $\mathcal{PT}$ symmetry, making bilayer MnSe globally $\mathcal{PT}$ symmetric [Fig. 1(e)]. Therefore, we say that α_i is the inversion partner of β_i. As a consequence, the state localized on the α_i sublayer $|\psi^{\alpha_i}_{\boldsymbol{k},\uparrow}\rangle$ and the state localized on β_i sublayer $|\psi^{\beta_i}_{\boldsymbol{k},\downarrow}\rangle$ are energy degenerate ($E^{\alpha_i}_{\boldsymbol{k},\uparrow} = E^{\beta_i}_{\boldsymbol{k},\downarrow}$). More importantly, the two components of doubly degenerate bands have opposite spin polarization ($S^{\alpha_i}_{\boldsymbol{k}} = -S^{\beta_i}_{\boldsymbol{k}}$), each spatially localized on one of the two separate sublayers forming the inversion partners, called the spin-sublayer locking effect [Fig. 2(c)]. When examining a specific layer (say α) [see Ref. [40] for the experimental procedure] that consists of sublayers α_1 and α_2, the states localized on α_1 and α_2 have nondegenerate energy. Consequently, the states $|\psi^{\alpha_1}_{\boldsymbol{k},\uparrow}\rangle$ and $|\psi^{\alpha_2}_{\boldsymbol{k},\downarrow}\rangle$ create a Zeeman pair. Similarly, β_1 and β_2 states also make a Zeeman pair. Moreover, the anticommutation relationship between M_x and $\sigma_{y,z}$ in spin space (where $\sigma_{x,y,z}$ represents the Pauli matrices) imposes a condition on the general energy eigenstate $|\psi^{\alpha_i/\beta_i}_{\boldsymbol{k},\uparrow/\downarrow}\rangle$. Specifically, $\langle\psi^{\alpha_i/\beta_i}_{\boldsymbol{k},\uparrow/\downarrow}|M_x^{-1}\sigma_{y,z}M_x|\psi^{\alpha_i/\beta_i}_{\boldsymbol{k},\uparrow/\downarrow}\rangle = -\langle\psi^{\alpha_i/\beta_i}_{\boldsymbol{k},\uparrow/\downarrow}|\sigma_{y,z}|\psi^{\alpha_i/\beta_i}_{\boldsymbol{k},\uparrow,\downarrow}\rangle$, which implies that $\langle\psi^{\alpha_i/\beta_i}_{\boldsymbol{k},\uparrow/\downarrow}|\sigma_{y,z}|\psi^{\alpha_i/\beta_i}_{\boldsymbol{k},\uparrow/\downarrow}\rangle = 0$. Consequently, the spin orientations are independent of $\boldsymbol{k}$ and aligned parallel or antiparallel to x direction. That leads to the HZSS with persistent spin textures [Fig. 2(c)], and the energy relationship can be expressed as

$$E^{\alpha_i}_{\boldsymbol{k},\uparrow} = E^{\beta_i}_{\boldsymbol{k},\downarrow}, \quad i = 1,2 \quad \text{and} \quad E^{s_1}_{\boldsymbol{k},\uparrow} \neq E^{s_2}_{\boldsymbol{k},\downarrow}, \quad s = \alpha, \beta. \quad (1)$$

Next, we apply an electric field ($\mathcal{E}$) to break $\mathcal{PT}$ symmetry. The electric field creates a net charge polarization ($\boldsymbol{P} \propto \boldsymbol{\mathcal{E}}$) [28]. Induced polarization generates a net magnetization ($M_i \propto P_j$) through the magnetoelectric effect [28], lifting the $\mathcal{PT}$ symmetry between inversion partners. The occurrence of magnetization induces an effective magnetic field ($\boldsymbol{B}^{\text{eff}} \propto \boldsymbol{P}$) that couples with the spin degrees of freedom, yielding a Zeeman-like Hamiltonian $\sum_{i,j}\lambda_{i,j}P_i\sigma_j$. Tensor $\lambda_{i,j}$ determines the strength of the magnetoelectric coupling. Some components of $\lambda_{i,j}$ are never nonzero and vanish due to the symmetry. We determine the symmetry-allowed terms λ_{ij} using the method of invariants [41] ($H = O^{\dagger}HO$, where O is the symmetry operation belonging to the MPG $2'/m$), generally used to determine the $\boldsymbol{k}\cdot\boldsymbol{p}$ Hamiltonian in nonmagnetic materials [42,43]. The Zeeman Hamiltonian (H_Z), following the transformation rules of P_i and σ_j listed in Table I, is given by

$$H_Z = \lambda_{x,y}P_x\sigma_y + \lambda_{x,z}P_x\sigma_z + \lambda_{y,x}P_y\sigma_x + \lambda_{z,x}P_z\sigma_x. \quad (2)$$

H_Z breaks the $\mathcal{PT}$ symmetry and lifts the energy degeneracy between states localized on inversion partners [Fig. 2(d)], thus forming additional Zeeman-like pairs

$$E^{\alpha_i}_{\boldsymbol{k},\uparrow} \neq E^{\beta_i}_{\boldsymbol{k},\downarrow}, \quad i = 1,2 \quad \text{and} \quad E^{s_1}_{\boldsymbol{k},\uparrow} \neq E^{s_2}_{\boldsymbol{k},\downarrow}, \quad s = \alpha, \beta. \quad (3)$$

TABLE I. The transformation rules of electric polarization (P_x, P_y, P_z) and Pauli spin matrices (σ_x, σ_y, σ_z) with respect to the operations (O) belonging to MPG $2'/m$. The last column shows the terms which are invariant under operation.

O	(P_x, P_y, P_z)	$(\sigma_x, \sigma_y, \sigma_z)$	Invariants
I	(P_x, P_y, P_z)	$(\sigma_x, \sigma_y, \sigma_z)$	$P_i\sigma_j(i, j = x, y, z)$
M_x	$(-P_x, P_y, P_z)$	$(\sigma_x, -\sigma_y, -\sigma_z)$	$P_x\sigma_{y/z}$, $P_{y/z}\sigma_x$
$C_{2x}\mathcal{T}$	$(P_x, -P_y, -P_z)$	$(-\sigma_x, \sigma_y, \sigma_z)$	$P_x\sigma_{y/z}$, $P_{y/z}\sigma_x$
$\mathcal{PT}$	$(-P_x, -P_y, -P_z)$	$(-\sigma_x, -\sigma_y, -\sigma_z)$	$P_i\sigma_j(i, j = x, y, z)$

It should be noted that H_Z is determined assuming that the magnetization axis aligns with the x direction. However, the Hamiltonian can be adapted for any in-plane direction by rotating it accordingly.

DFT analysis. According to symmetry analysis, there are two conditions to observe HZSS: (i) global $\mathcal{PT}$ symmetry and (ii) the states segregated on the local $\mathcal{PT}$-asymmetric sites. Condition (i) is already fulfilled, and to check condition (ii), we plot the orbital-projected band structure of bilayer MnSe considering spin-orbit interaction [Fig. 3(a)]. Under C_{3v} site symmetry, the Mn-d orbitals split into three categories, d_{z^2}, $(d_{x^2-y^2}, d_{xy})$, and (d_{xz}, d_{yz}). The Se-p orbitals are split into two categories, p_z and (p_x, p_y). The Mn-d orbitals form conduction band (CB) states, while Se-p orbitals mainly contribute to valence band (VB) states. Compared to the band structure of monolayer MnSe [Fig. 1(f)], interlayer interaction between inversion partners α_1 and α_2 results in increased separation between the nested bands and spin mixture from another sublayer. Compared to the in-plane orbitals ($d_{x^2-y^2}$, d_{xy}, p_x, p_y), the out-of-plane orbitals (d_{xz}, d_{yz}, d_{z^2}, p_z) exhibit significant interlayer and intersublayer interaction (see Sec. II of the SM [38]). Observing HZSS is not ideal with the CB states around the M and Γ points and the VB states around the

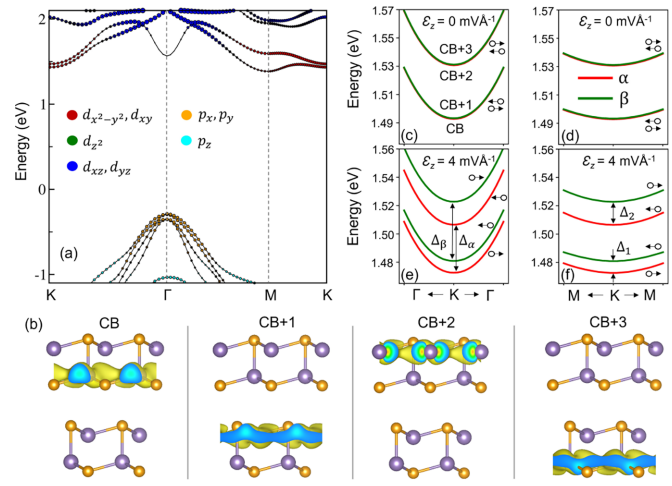

FIG. 3. (a) Orbital-projected band dispersion curves of bilayer MnSe with AB stacking. (b) $|\psi_{nk}(\boldsymbol{r})|^2$ for the states CB, CB + 1, CB + 2, and CB + 3 at the K point. Layer-projected CBs of bilayer MnSe around the K point along (c) K-Γ and (d) K-M. (e)–(f) Counterparts of (c)–(d) in the presence of a small electric field of 4 mVÅ^{-1} along the z direction.

K and M points. That is because these states have contributions from the hybridization of out-of-plane orbitals between different sublayers, and thus their wave functions are not segregated. The CB states near the K point are predominantly contributed by $(d_{x^2-y^2}, d_{xy})$, and VB states around the Γ point are composed of mainly (p_x, p_y). Therefore states arising from the in-plane orbitals, i.e., the CBs near the K point and the VBs near the Γ point, have weak communication between different sublayers, leading to minimal separation between nested bands and spin mixture from neighboring layers. Consequently, each wave function is localized within the sublayer for the CBs near the K point and the VBs near the Γ point, forming the ideal choice to observe the spin-sublayer locking effect and HZSS [Fig. 3(b)].

Next, we plot layer-projected dispersion curves for low CBs in the vicinity of the K point for bilayer MnSe [Figs. 3(c) and 3(d)]. The four lowest CBs form two twofold degenerate pairs [see Eq. (1)]. Despite having the same energy, these states are localized on distinct sublayers and can be probed using $\boldsymbol{r}$-resolved spectroscopy techniques [7,44]. For instance, the degenerate states CB and CB + 1 segregate on inversion partners α_1 and β_1, respectively [Fig. 3(b)]. Both inversion partners possess finite and opposite $\boldsymbol{k}$-independent spin orientations, either parallel or antiparallel to the x direction (see Sec. III of the SM [38]), ensuring zero net spin polarization respecting the $\mathcal{PT}$ symmetry requirement. The k-independent persistent spin textures overcome spin dephasing and provide nondissipative spin transport [45–47]. The α_1 sublayer has a magnetization of magnitude $4.38\mu_B$ along $+x$ direction and is compensated by the opposite magnetization of inversion partner β_1. A similar analysis also applies to the upper degenerate pair CB + 2 and CB + 3, where wave functions corresponding to CB + 2 and CB + 3 have segregated on α_2 and β_2 sublayers, respectively. If we focus locally on each layer, $(|\psi^{\alpha_1}_{K,\uparrow}\rangle, |\psi^{\alpha_2}_{K,\downarrow}\rangle)$ and $(|\psi^{\beta_1}_{K,\downarrow}\rangle, |\psi^{\beta_2}_{K,\uparrow}\rangle)$ form two Zeeman pairs with energy splittings Δ_α, Δ_β, respectively [Figs. 3(c) and 3(d)]. As a consequence of $\mathcal{PT}$ symmetry, the strength of the Zeeman spin splitting is the same for each layer ($\Delta_\alpha = \Delta_\beta$) to satisfy the Kramers degeneracy. We have observed Zeeman spin splitting of order ∼39.5 meV. Observed Zeeman splitting in our case (without external fields) is comparable to bulk AFM semiconductors Fe_2TeO_6 (55 meV) and $SrFe_2S_2O$ (33 meV) under an external electric field of strength 60 mVÅ^{-1} [27]. However, it is still smaller than that of nonmagnetic transition metal dichalcogenides, i.e., MoS_2 (150 meV) [48]. HZSS is also observed for the VB states near the Γ point, where both α and β bands are Zeeman split (Δ_α, Δ_β) by ∼70 meV, as discussed in Sec. IV of the SM [38].

Effect of external electric field. The H_Z expressed in Eq. (2) shows that twofold degeneracy will be lifted by including polarization along an arbitrary direction (P_x, P_y, P_z). We include P_z through the application of an electric field along the z direction ($\mathcal{E}_z$), and our model in Eq. (2) can readily be generalized to

$$H_Z = \gamma_{z,x}\mathcal{E}_z\sigma_x \tag{4}$$

where $\gamma_{z,x}$ determines the strength of splitting. We plot the CBs in a tiny $\mathcal{E}_z$ of 4 mVÅ^{-1} [Figs. 3(e) and 3(f)]. The

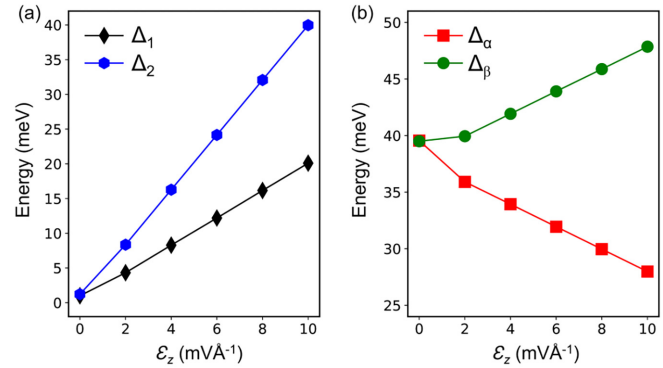

FIG. 4. The Zeeman spin splittings for the CBs (a) Δ_1, Δ_2 and (b) Δ_α, Δ_β in bilayer MnSe as a function of electric field $\mathcal{E}_z$.

$\mathcal{E}_z$ creates an asymmetric potential on the inversion partners sublayers, resulting in global $\mathcal{PT}$ symmetry breaking. Each degenerate pair splits into two levels $E_+ = \gamma_{z,x}\mathcal{E}_z$ (eigenstate being $|+\rangle$) and $E_- = -\gamma_{z,x}\mathcal{E}_z$ (eigenstate being $|-\rangle$), where $\sigma_x|+\rangle = +|+\rangle$ and $\sigma_x|-\rangle = -|-\rangle$. Therefore, two degenerate pairs in bilayer MnSe split into four energy levels, as represented by the Δ_1 and Δ_2 in Fig. 3(f). Here Δ_1 (Δ_2) represents the energy difference between the state localized on the α_1 (α_2), and the state localized on β_1 (β_2). Upon initial observation, it is evident that $\Delta_1 < \Delta_2$ due to the smaller real space separation between α_1 and β_1 compared to that between α_2 and β_2. Consequently, this results in a lesser potential difference between α_1 and β_1, leading to a smaller energy splitting Δ_1 compared to Δ_2.

After that, we plot energy splittings (Δ_1, Δ_2, Δ_α, and Δ_β) as a function of the $\mathcal{E}_z$ [Figs. 4(a) and 4(b)]. We notice that the energy splittings show a linear dependence on the $\mathcal{E}_z$ in the range of 0 to 10 mVÅ^{-1}. Maximum Δ_1 and Δ_2 are observed to be 20.0 and 39.9 meV, respectively, with the $\mathcal{E}_z$ of strength 10 mVÅ^{-1}. The $\mathcal{E}_z$ breaks the equality between Δ_α and Δ_β, where Δ_α decreases and Δ_β increases with increasing strength of the $\mathcal{E}_z$. The observed strength of Δ_α and Δ_β are 28.0 and 47.8 meV, respectively, under the influence of 10 mVÅ^{-1} $\mathcal{E}_z$. Additionally, the reversal of the electric field from $\mathcal{E}_z$ to $-\mathcal{E}_z$ will reverse the spin magnetization S_x to $-S_x$ (see Sec. V of the SM [38]). Under an electric field of the same magnitude along the $+z$ or $-z$ direction, the strength of splittings $|\Delta_1|$ and $|\Delta_2|$ is independent of the electric field direction. However, Δ_1 and Δ_2 will flip their sign under electric field reversal. These results are in qualitative agreement with our model Hamiltonian H_z in Eq. (4). If we compare the effect of the electric field on bilayer MnSe with monolayer MnSe [Fig. 1(f)], we find that a large electric field is required in monolayer MnSe to obtain the Zeeman splitting of the same order. More specifically, Zeeman split pair of 50.9 meV is observed with $\mathcal{E}_z$ of strength 50 mVÅ^{-1}. Also, Zeeman splitting without any external field in bilayer MnSe is an additional advantage over monolayer MnSe.

It is interesting to note that $\mathcal{PT}$ symmetry remains intact with increasing layer thickness. Therefore, effects similar to bilayer MnSe are also achieved in trilayer and tetralayer MnSe, where every band is doubly degenerate, and degenerate pair of bands are localized on different sublayers connected

through $\mathcal{PT}$ symmetry (see Sec. VI of SM [38]). Thus, experimental realization of HZSS can be easily achieved in layered MnSe with arbitrary thickness.

In conclusion, we have shown the existence of HZSS in bilayer MnSe, combining first-principles calculations and symmetry analysis. The stacking characteristic study shows that AB with $\mathcal{PT}$ symmetry is the lowest energy stacking. The doubly degenerate states arising due to $\mathcal{PT}$ symmetry are segregated into different sublayers forming inversion partners. Then, we identified the local Zeeman splitting as large as ∼70 meV in bilayer MnSe, where states forming Zeeman pair with opposite spin orientation segregate on different sublayers within a single layer. Interestingly, a tiny out-of-plane electric field yields additional Zeeman pairs through breaking twofold degeneracy. M_x enforced persistence spin textures remain preserved under an out-of-plane electric field and are known for nondissipative spin transport. Moreover, the fact that our results are independent of the layer number adds credibility to the possibility of experimental observation. Controllable Zeeman spin splittings achieved using electric fields are detectable through established approaches such as optical and transport measurements commonly used in spintronics [49,50]. Zeeman splittings with hidden spin polarization in centrosymmetric antiferromagnets form another prospective aspect in developing semiconductor spintronics devices [51]. We anticipate that our findings will contribute to a deeper understanding of magnetoelectric interactions and broaden the emerging fields of AFM and semiconductor spintronics [52,53].

Acknowledgments. S.S. acknowledges CSIR, India, for support via a senior research fellowship [Grant No. 09/086(1432)/2019-EMR-I]. S.B. acknowledges financial support from SERB under a core research grant (Grant No. CRG/2019/000647) to set up his High-Performance Computing (HPC) facility "Veena" at IIT Delhi for computational resources.

[1] G. Dresselhaus, Spin-orbit coupling effects in zinc blende structures, Phys. Rev. **100**, 580 (1955).

[2] E. Rashba, Properties of semiconductors with an extremum loop. I. Cyclotron and combinational resonance in a magnetic field perpendicular to the plane of the loop, Sov. Phys. Solid State **2**, 1109 (1960).

[3] F. Vasko, Spin splitting in the spectrum of two-dimensional electrons due to the surface potential, Sov. J. Exp. Theor. Phys. Lett. **30**, 541 (1979).

[4] Y. A. Bychkov and É. I. Rashba, Properties of a 2D electron gas with lifted spectral degeneracy, JETP Lett. **39**, 78 (1984).

[5] X. Zhang, Q. Liu, J.-W. Luo, A. J. Freeman, and A. Zunger, Hidden spin polarization in inversion-symmetric bulk crystals, Nat. Phys. **10**, 387 (2014).

[6] R. Bertoni, C. W. Nicholson, L. Waldecker, H. Hübener, C. Monney, U. De Giovannini, M. Puppin, M. Hoesch, E. Springate, R. T. Chapman *et al.*, Generation and evolution of spin-, valley-, and layer-polarized excited carriers in inversion-symmetric WSe_2, Phys. Rev. Lett. **117**, 277201 (2016).

[7] W. Yao, E. Wang, H. Huang, K. Deng, M. Yan, K. Zhang, K. Miyamoto, T. Okuda, L. Li, Y. Wang *et al.*, Direct observation of spin-layer locking by local Rashba effect in monolayer semiconducting $PtSe_2$ film, Nat. Commun. **8**, 14216 (2017).

[8] L. Yuan, Q. Liu, X. Zhang, J.-W. Luo, S.-S. Li, and A. Zunger, Uncovering and tailoring hidden Rashba spin–orbit splitting in centrosymmetric crystals, Nat. Commun. **10**, 906 (2019).

[9] Y. Huang, A. Yartsev, S. Guan, L. Zhu, Q. Zhao, Z. Yao, C. He, L. Zhang, J. Bai, J. W. Luo, and X. Xu, Hidden spin polarization in the centrosymmetric MoS_2 crystal revealed via elliptically polarized terahertz emission, Phys. Rev. B **102**, 085205 (2020).

[10] O. J. Clark, O. Dowinton, M. S. Bahramy, and J. Sánchez-Barriga, Hidden spin-orbital texture at the γ-located valence band maximum of a transition metal dichalcogenide semiconductor, Nat. Commun. **13**, 4147 (2022).

[11] X.-F. Qian, T. Malhotra, A. N. Vamivakas, and J. H. Eberly, Coherence constraints and the last hidden optical coherence, Phys. Rev. Lett. **117**, 153901 (2016).

[12] Q. Liu, X. Zhang, and A. Zunger, Intrinsic circular polarization in centrosymmetric stacks of transition-metal dichalcogenide compounds, Phys. Rev. Lett. **114**, 087402 (2015).

[13] J. H. Ryoo and C.-H. Park, Hidden orbital polarization in diamond, silicon, germanium, gallium arsenide and layered materials, NPG Asia Mater. **9**, e382 (2017).

[14] S. Beaulieu, J. Schusser, S. Dong, M. Schüler, T. Pincelli, M. Dendzik, J. Maklar, A. Neef, H. Ebert, K. Hricovini *et al.*, Revealing hidden orbital pseudospin texture with time-reversal dichroism in photoelectron angular distributions, Phys. Rev. Lett. **125**, 216404 (2020).

[15] S. Cho, J.-H. Park, J. Hong, J. Jung, B. S. Kim, G. Han, W. Kyung, Y. Kim, S.-K. Mo, J. D. Denlinger, J. H. Shim, J. H. Han, C. Kim, and S. R. Park, Experimental observation of hidden berry curvature in inversion-symmetric bulk $2H$-WSe_2, Phys. Rev. Lett. **121**, 186401 (2018).

[16] M. Schüler, U. De Giovannini, H. Hübener, A. Rubio, M. A. Sentef, and P. Werner, Local berry curvature signatures in dichroic angle-resolved photoelectron spectroscopy from two-dimensional materials, Sci. Adv. **6**, eaay2730 (2020).

[17] Q. Liu, X. Zhang, H. Jin, K. Lam, J. Im, A. J. Freeman, and A. Zunger, Search and design of nonmagnetic centrosymmetric layered crystals with large local spin polarization, Phys. Rev. B **91**, 235204 (2015).

[18] J. Železný, P. Wadley, K. Olejník, A. Hoffmann, and H. Ohno, Spin transport and spin torque in antiferromagnetic devices, Nat. Phys. **14**, 220 (2018).

[19] P. Němec, M. Fiebig, T. Kampfrath, and A. V. Kimel, Antiferromagnetic opto-spintronics, Nat. Phys. **14**, 229 (2018).

[20] L.-D. Yuan, Z. Wang, J.-W. Luo, and A. Zunger, Prediction of low-Z collinear and noncollinear antiferromagnetic compounds having momentum-dependent spin splitting even without spin-orbit coupling, Phys. Rev. Mater. **5**, 014409 (2021).

[21] L.-D. Yuan, Z. Wang, J.-W. Luo, and A. Zunger, Strong influence of nonmagnetic ligands on the momentum-dependent spin splitting in antiferromagnets, Phys. Rev. B **103**, 224410 (2021).

[22] R. He, D. Wang, N. Luo, J. Zeng, K.-Q. Chen, and L.-M. Tang, Nonrelativistic spin-momentum coupling in antiferromagnetic twisted bilayers, Phys. Rev. Lett. **130**, 046401 (2023).

[23] L.-D. Yuan and A. Zunger, Degeneracy removal of spin bands in collinear antiferromagnets with non-interconvertible spin-structure motif pair, Adv. Mater. **35**, 2211966 (2023).

[24] H. Bai, L. Han, X. Y. Feng, Y. J. Zhou, R. X. Su, Q. Wang, L. Y. Liao, W. X. Zhu, X. Z. Chen, F. Pan, X. L. Fan, and C. Song, Observation of spin splitting torque in a collinear antiferromagnet RuO_2, Phys. Rev. Lett. **128**, 197202 (2022).

[25] N. Sivadas, S. Okamoto, and D. Xiao, Gate-controllable magneto-optic Kerr effect in layered collinear antiferromagnets, Phys. Rev. Lett. **117**, 267203 (2016).

[26] S. Li, T. Liu, C. Liu, Y. Wang, H.-Z. Lu, and X. C. Xie, Progress on the antiferromagnetic topological insulator $MnBi_2Te_4$, Natl. Sci. Rev. **11**, nwac296 (2024).

[27] H. J. Zhao, X. Liu, Y. Wang, Y. Yang, L. Bellaiche, and Y. Ma, Zeeman effect in centrosymmetric antiferromagnetic semiconductors controlled by an electric field, Phys. Rev. Lett. **129**, 187602 (2022).

[28] M. Fiebig, Revival of the magnetoelectric effect, J. Phys. D **38**, R123 (2005).

[29] J. Cao, W. Jiang, X.-P. Li, D. Tu, J. Zhou, J. Zhou, and Y. Yao, In-plane anomalous hall effect in $\mathcal{PT}$-symmetric antiferromagnetic materials, Phys. Rev. Lett. **130**, 166702 (2023).

[30] G. Kresse and D. Joubert, From ultrasoft pseudopotentials to the projector augmented-wave method, Phys. Rev. B **59**, 1758 (1999).

[31] G. Kresse and J. Furthmüller, Efficient iterative schemes for *ab initio* total-energy calculations using a plane-wave basis set, Phys. Rev. B **54**, 11169 (1996).

[32] J. P. Perdew, K. Burke, and M. Ernzerhof, Generalized gradient approximation made simple, Phys. Rev. Lett. **77**, 3865 (1996).

[33] A. I. Liechtenstein, V. I. Anisimov, and J. Zaanen, Density-functional theory and strong interactions: Orbital ordering in Mott-Hubbard insulators, Phys. Rev. B **52**, R5467 (1995).

[34] M. Aapro, M. N. Huda, J. Karthikeyan, S. Kezilebieke, S. C. Ganguli, H. G. Herrero, X. Huang, P. Liljeroth, and H.-P. Komsa, Synthesis and properties of monolayer mnse with unusual atomic structure and antiferromagnetic ordering, ACS Nano **15**, 13794 (2021).

[35] S. Sattar, M. F. Islam, and C. M. Canali, Monolayer Mn X and Janus X Mn Y ($X, Y =$ S, Se, Te): A family of two-dimensional antiferromagnetic semiconductors, Phys. Rev. B **106**, 085410 (2022).

[36] K. Liu, X. Ma, S. Xu, Y. Li, and M. Zhao, Tunable sliding ferroelectricity and magnetoelectric coupling in two-dimensional multiferroic MnSe materials, npj Comput. Mater. **9**, 16 (2023).

[37] J. Neugebauer and M. Scheffler, Adsorbate-substrate and adsorbate-adsorbate interactions of Na and K adlayers on Al(111), Phys. Rev. B **46**, 16067 (1992).

[38] See Supplemental Material at http://link.aps.org/supplemental/10.1103/PhysRevB.109.L020404 for computational methods, wave-function analysis, spin textures, HZSS for the valence bands around the Γ point, electric field reversal, and extension to multilayers, which also includes Refs. [30–34,37,46,53–68].

[39] G. Constantinescu, A. Kuc, and T. Heine, Stacking in bulk and bilayer hexagonal boron nitride, Phys. Rev. Lett. **111**, 036104 (2013).

[40] W. Lee, S. Fernandez-Mulligan, H. Tan, C. Yan, Y. Guan, S. H. Lee, R. Mei, C. Liu, B. Yan, Z. Mao *et al.*, Layer-by-layer disentanglement of bloch states, Nat. Phys. **19**, 950 (2023).

[41] L. C. L. Y. Voon and M. Willatzen, *The $k \cdot p$ Method: Electronic Properties of Semiconductors* (Springer, Berlin, 2009).

[42] L. L. Tao, T. R. Paudel, A. A. Kovalev, and E. Y. Tsymbal, Reversible spin texture in ferroelectric HfO_2, Phys. Rev. B **95**, 245141 (2017).

[43] S. Sheoran, S. Monga, A. Phutela, and S. Bhattacharya, Coupled spin-valley, rashba effect, and hidden spin polarization in WSi_2N_4 family, J. Phys. Chem. Lett. **14**, 1494 (2023).

[44] H. Lu, Z. Qi, Y. Huang, M. Cheng, F. Sheng, Z. Deng, S. Chen, C. Hua, P. He, Y. Lu *et al.*, Unlocking hidden spins in centrosymmetric 1T transition metal dichalcogenides by vacancy-controlled spin-orbit scattering, Phys. Rev. B **107**, 165419 (2023).

[45] L. Tao and E. Y. Tsymbal, Persistent spin texture enforced by symmetry, Nat. Commun. **9**, 2763 (2018).

[46] H. J. Zhao, H. Nakamura, R. Arras, C. Paillard, P. Chen, J. Gosteau, X. Li, Y. Yang, and L. Bellaiche, Purely cubic spin splittings with persistent spin textures, Phys. Rev. Lett. **125**, 216405 (2020).

[47] S. Sheoran, P. Bhumla, and S. Bhattacharya, Emergence of cubic ordered full-plane persistent spin textures in lead-free materials, Phys. Rev. Mater. **6**, 094602 (2022).

[48] D. Xiao, G.-B. Liu, W. Feng, X. Xu, and W. Yao, Coupled spin and valley physics in monolayers of MoS_2 and other group-VI dichalcogenides, Phys. Rev. Lett. **108**, 196802 (2012).

[49] X. Zhang, H.-O. Li, G. Cao, M. Xiao, G.-C. Guo, and G.-P. Guo, Semiconductor quantum computation, Natl. Sci. Rev. **6**, 32 (2019).

[50] D.-F. Shao, Y.-Y. Jiang, J. Ding, S.-H. Zhang, Z.-A. Wang, R.-C. Xiao, G. Gurung, W. J. Lu, Y. P. Sun, and E. Y. Tsymbal, Néel spin currents in antiferromagnets, Phys. Rev. Lett. **130**, 216702 (2023).

[51] W. Chen, M. Gu, J. Li, P. Wang, and Q. Liu, Role of hidden spin polarization in nonreciprocal transport of antiferromagnets, Phys. Rev. Lett. **129**, 276601 (2022).

[52] V. Baltz, A. Manchon, M. Tsoi, T. Moriyama, T. Ono, and Y. Tserkovnyak, Antiferromagnetic spintronics, Rev. Mod. Phys. **90**, 015005 (2018).

[53] O. Gomonay, V. Baltz, A. Brataas, and Y. Tserkovnyak, Antiferromagnetic spin textures and dynamics, Nat. Phys. **14**, 213 (2018).

[54] S. Grimme, Semiempirical GGA-type density functional constructed with a long-range dispersion correction, J. Comput. Chem. **27**, 1787 (2006).

[55] M. S. Dresselhaus, G. Dresselhaus, and A. Jorio, *Group Theory: Application to the Physics of Condensed Matter* (Springer, Berlin, 2007).

[56] M. I. Aroyo, J. M. Perez-Mato, C. Capillas, E. Kroumova, S. Ivantchev, G. Madariaga, A. Kirov, and H. Wondratschek, Bilbao crystallographic server: I. Databases and crystallographic computing programs, Z. Kristallogr. Cryst. Mater. **221**, 15 (2006).

[57] L. Elcoro, B. Bradlyn, Z. Wang, M. G. Vergniory, J. Cano, C. Felser, B. A. Bernevig, D. Orobengoa, G. Flor, and M. I. Aroyo, Double crystallographic groups and their representations on the

Bilbao crystallographic server, J. Appl. Crystallogr. **50**, 1457 (2017).

[58] H. T. Stokes and D. M. Hatch, Findsym: program for identifying the space-group symmetry of a crystal, J. Appl. Crystallogr. **38**, 237 (2005).

[59] Y. Hinuma, G. Pizzi, Y. Kumagai, F. Oba, and I. Tanaka, Band structure diagram paths based on crystallography, Comput. Mater. Sci. **128**, 140 (2017).

[60] V. Wang, N. Xu, J.-C. Liu, G. Tang, and W.-T. Geng, Vaspkit: A user-friendly interface facilitating high-throughput computing and analysis using VASP code, Comput. Phys. Commun. **267**, 108033 (2021).

[61] U. Herath, P. Tavadze, X. He, E. Bousquet, S. Singh, F. Muñoz, and A. H. Romero, Pyprocar: A Python library for electronic structure pre/post-processing, Comput. Phys. Commun. **251**, 107080 (2020).

[62] S. V. Gallego, J. M. Perez-Mato, L. Elcoro, E. S. Tasci, R. M. Hanson, K. Momma, M. I. Aroyo, and G. Madariaga, MAGNDATA: Towards a database of magnetic structures. I. The commensurate case, J. Appl. Crystallogr. **49**, 1750 (2016).

[63] J. Schliemann, Colloquium: Persistent spin textures in semiconductor nanostructures, Rev. Mod. Phys. **89**, 011001 (2017).

[64] S. Bhattacharya and Y. Kanai, Spin-orbit-coupling-induced band splitting in two-dimensional hybrid organic-inorganic perovskites: Importance of organic cations, Phys. Rev. Mater. **7**, 055001 (2023).

[65] C. H. Lui, Z. Li, K. F. Mak, E. Cappelluti, and T. F. Heinz, Observation of an electrically tunable band gap in trilayer graphene, Nat. Phys. **7**, 944 (2011).

[66] K. G. Wirth, J. B. Hauck, A. Rothstein, H. Kyoseva, D. Siebenkotten, L. Conrads, L. Klebl, A. Fischer, B. Beschoten, C. Stampfer *et al.*, Experimental observation of ABCB stacked tetralayer graphene, ACS Nano **16**, 16617 (2022).

[67] P. Meng, Y. Wu, R. Bian, E. Pan, B. Dong, X. Zhao, J. Chen, L. Wu, Y. Sun, Q. Fu *et al.*, Sliding induced multiple polarization states in two-dimensional ferroelectrics, Nat. Commun. **13**, 7696 (2022).

[68] Y. Zhao, X. Luo, H. Li, J. Zhang, P. T. Araujo, C. K. Gan, J. Wu, H. Zhang, S. Y. Quek, M. S. Dresselhaus *et al.*, Interlayer breathing and shear modes in few-trilayer MoS_2 and WSe_2, Nano Lett. **13**, 1007 (2013).